



Publication Year	2018
Acceptance in OA	2020-10-27T10:20:16Z
Title	Mercury Hollows as Remnants of Original Bedrock Materials and Devolatilization Processes: A Spectral Clustering and Geomorphological Analysis
Authors	LUCCHETTI, ALICE, PAJOLA, MAURIZIO, GALLUZZI, VALENTINA, Giacomini, L., CARLI, CRISTIAN, CREMONESE, Gabriele, Marzo, G. A., Ferrari, S., Massironi, M., PALUMBO, PASQUALE
Publisher's version (DOI)	10.1029/2018JE005722
Handle	http://hdl.handle.net/20.500.12386/28017
Journal	JOURNAL OF GEOPHYSICAL RESEARCH (PLANETS)
Volume	123

RESEARCH ARTICLE

10.1029/2018JE005722

Key Points:

- Spectral behavior of hollows is identified by a wide absorption band between 0.558 and 0.828 μm , with a hint of absorption toward 1 μm
- The hollow absorption can be explained by pyroxenes presenting transitional elements, in addition to sulfides
- Hollows consist of both the remnant material coming from a degassing process and the bedrock-forming material in which they formed

Supporting Information:

- Supporting Information S1
- Table S1
- Table S2
- Table S3

Correspondence to:

A. Lucchetti,
alice.lucchetti@inaf.it

Citation:

Lucchetti, A., Pajola, M., Galluzzi, V., Giacomini, L., Carli, C., Cremonese, G., et al. (2018). Mercury hollows as remnants of original bedrock materials and devolatilization processes: A spectral clustering and geomorphological analysis. *Journal of Geophysical Research: Planets*, 123, 2365–2379. <https://doi.org/10.1029/2018JE005722>

Received 18 JUN 2018

Accepted 9 AUG 2018

Accepted article online 22 AUG 2018

Published online 17 SEP 2018

The version of record includes the crater name, Canova. This replaces the previously Unnamed crater in the Accepted Article version of this paper. The name was added after approval from the International Astronomical Union on September 5, 2018.

Mercury Hollows as Remnants of Original Bedrock Materials and Devolatilization Processes: A Spectral Clustering and Geomorphological Analysis

A. Lucchetti¹ , M. Pajola¹ , V. Galluzzi² , L. Giacomini², C. Carli² , G. Cremonese¹, G. A. Marzo³, S. Ferrari⁴, M. Massironi⁵, and P. Palumbo⁶

¹INAF-OAPD, Astronomical Observatory of Padova, Padova, Italy, ²INAF-IAPS, Istituto di Astrofisica e Planetologia Spaziali, Rome, Italy, ³ENEA Centro Ricerche Casaccia, Rome, Italy, ⁴CISAS, University of Padova, Padova, Italy, ⁵Department of Geosciences, University of Padova, Padova, Italy, ⁶Dipartimento di Scienze e Tecnologie, Università di Napoli "Parthenope", Napoli, Italy

Abstract We perform a detailed geomorphological and compositional analysis on three craters hosting hollows located in the Victoria and Kuiper Quadrangles of Mercury. Based on Mercury Dual Imaging System data, high-resolution detailed geomorphological mapping is provided in order to fully characterize the geological framework where hollows formed. In addition, we apply an unsupervised spectral clustering, based on a K-mean algorithm, to separate in clusters our data sets. The comparison between the spectral and the well-defined geomorphological units reveals a spatially coherent distribution. In particular, all hollows are uniquely identified by a well-defined spectrum showing a wide absorption band between 0.558 and 0.828, with a possible hint of absorption toward 1 μm . Our analysis suggests that the composition of hollows may be characterized by a mixture of different minerals contributing to the absorptions found in our spectra. Indeed, sulfides alone (CaS, MnS, and MgS) cannot explain the spectrum behavior of hollows, even if the mechanism forming hollows likely involves the loss of volatiles from the surface. Hence, we have to consider bedrock-forming material as partial responsible of the absorptions. For the studied hollows we suggest that the bedrock-forming minerals are pyroxenes presenting transitional elements, like Cr, Ti, and Ni in substitution of Mg and/or Fe. Therefore, we suggest that the spectral characteristics of hollows are related to both remnant material produced by devolatilization process and to bedrock in which the hollows formed.

Plain Language Summary The Mercury Surface, Space ENvironment, GEochemistry, and Ranging mission provided the first detailed view of Mercury's surface and its space environment. Among the many discoveries, it revealed for the first time the presence of unusual bright irregular and rimless flat-floored depression, called hollows, which are usually found on crater walls, rims, floors, and central peaks. Understanding the nature of hollows is still a major challenge since it is difficult to define which is their source mechanism. By using multicolor images acquired through the Mercury Dual Imaging System, we analyzed the nature of hollows hosted by three different impact craters, both from a geomorphological and a compositional perspective. Such analysis revealed that different units identified in high-resolution geological maps are characterized by different spectral behaviors. Hollows in all craters have a well-defined visible spectrum that when compared with laboratory spectra is indicative of the presence of both sulfides and pyroxene presenting transitional elements. This provides new insights into the hollows' nature and composition, suggesting that hollow terrains are the expression of both the remnant material coming from a process that involve devolatilization and the bedrock-forming material (planet crust) where they formed.

1. Introduction

One of the most surprising discoveries revealed by the MESSENGER (Mercury Surface, Space, Environment, Geochemistry, and Ranging, Solomon, 2011; Solomon et al., 2007) spacecraft was the presence of peculiar features, called hollows, on the surface of Mercury. In the 1970s, the Mariner 10 spacecraft already imaged such features, but it was only when MESSENGER went into orbit in 2011 that both high-resolution and multi-spectral images made possible a detailed analysis of hollows.

These features were revealed as shallow irregular and rimless flat-floored depressions with bright interiors and halos, often found on crater walls, rims, floors, and central peaks (Blewett et al., 2011, 2013; Thomas

et al., 2014). Their size ranges from tens of meters across for individual hollows to tens of kilometers across when clusters of hollows are present (Blewett et al., 2011). The hollows are scattered all over the surface, but they are likely controlled by several factors, such as the intensity of insolation or the substrate composition (Thomas et al., 2014). Moreover, since they appear fresh, they may be actively forming today via a mechanism that could involve depletion of subsurface volatiles (Blewett et al., 2011; Vaughan et al., 2012), whose nature is not yet known. Indeed, there are multiple candidates for these volatiles, such as chlorides or sulfurs (Blewett et al., 2013; Helbert et al., 2013; Vaughan et al., 2012), even though the data on elemental composition provided by MESSENGER do not have sufficient spatial resolution to assess the nature of this material at the scale of hollows (Evans et al., 2012; Goldsten et al., 2007; Hawkins et al., 2007; Nittler et al., 2011; Peplowski et al., 2011; Schlemm et al., 2007; Weider et al., 2012). Hollows are usually found in correspondence of low reflectance material (LRM), which is a major global color-composition unit mapped over large areas of the planet (Denevi et al., 2009). The LRM has been suggested to have originated at depth within Mercury's crust and could be the result of accumulation of endogenic carbon, potentially sourced from the remnants of a magma ocean flotation crust (Klima et al., 2018; Vander Kaaden & McCubbin, 2015). Hence, it is thought to be the volatile-bearing unit that degrades forming hollows (Thomas et al., 2014). This suggests a possible connection between the hollows formation and the phase responsible for darkening the LRM (Gillis-Davis et al., 2013; Lucey & Riner, 2011; Murchie et al., 2015).

The morphological observations of hollows suggest that these features may not be controlled by a single forming event (Blewett et al., 2011; Thomas et al., 2014). Hence, several processes have been suggested for the possible release of volatiles (Blewett et al., 2011) such as sublimation, thermal desorption, photon stimulated desorption, chemical sputtering, micrometeorite impact vaporization, and pyroclastic volcanism. Recently, another mechanism for the volatile release involving the destruction of graphite by proton bombardment has been proposed (Blewett et al., 2016). From a compositional perspective, Vilas et al. (2016) identified an absorption feature extending from 0.559 to 0.828 μm in the photometry of hollows located in the center of the Dominici crater (1.38 N, 323.5°E) and one centered at 0.629 μm in the crater's south wall/rim. These absorptions suggest the presence of MgS or a combination of MgS and CaS. Therefore, assessing the compositional character of hollows is fundamental to constraining origin of these features and, consequently, for understanding the whole Mercurian surface.

In this work, we characterize in deeper detail the morphological characteristics and the spectral properties of hollows located in three different craters. We perform high-resolution detailed geomorphological mapping in order to fully provide the geological framework where these features formed. In addition, we apply to our data sets a spectral clustering technique based on a K-mean algorithm that allows us to identify spectrally similar regions (characterized by an average multicolor spectrum) of the studied areas. Then, we compare our spectrum results with the high-resolution geomorphological maps, identifying a strong correlation between the spectral behavior of hollows and the geomorphological units. Finally, we find similar spectral trends between the studied hollows and compare them with laboratory spectra to provide hints on the material's origin.

2. Data Set and Methods

When MESSENGER went into orbit around Mercury in 2011, the MDIS (Mercury Dual Imaging System, Hawkins et al., 2007) instrument collected images with much higher resolution than those acquired during flybys, providing high-resolution targeted observations, coupled with global monochrome and multispectral base maps. The MDIS instrument consists of the wide angle camera (WAC), with a 10.5° field of view, and the narrow angle camera (NAC), with a 1.5° field of view. We use both WAC multispectral images and WAC and NAC monochrome images to provide detailed geomorphological map of craters hosting hollows and to characterize the spectral behavior of these features. We chose three different craters hosting hollows to enlarge the statistic of our results (Figure 1): (i) the Dominici crater (1.38°N, 36.5°W, Kuiper quadrangle, 20-km diameter), showing hollows both in the center and in the south crater wall/rim; (ii) the Canova crater (25.62°N, 3.75°W Victoria quadrangle, 25-km diameter), showing hollows on the northern part of its floor; and (iii) the Velazquez crater (37.74°N, 55.3°W Victoria quadrangle, 125-km diameter), presenting hollows mainly located on the top of its peak ring.

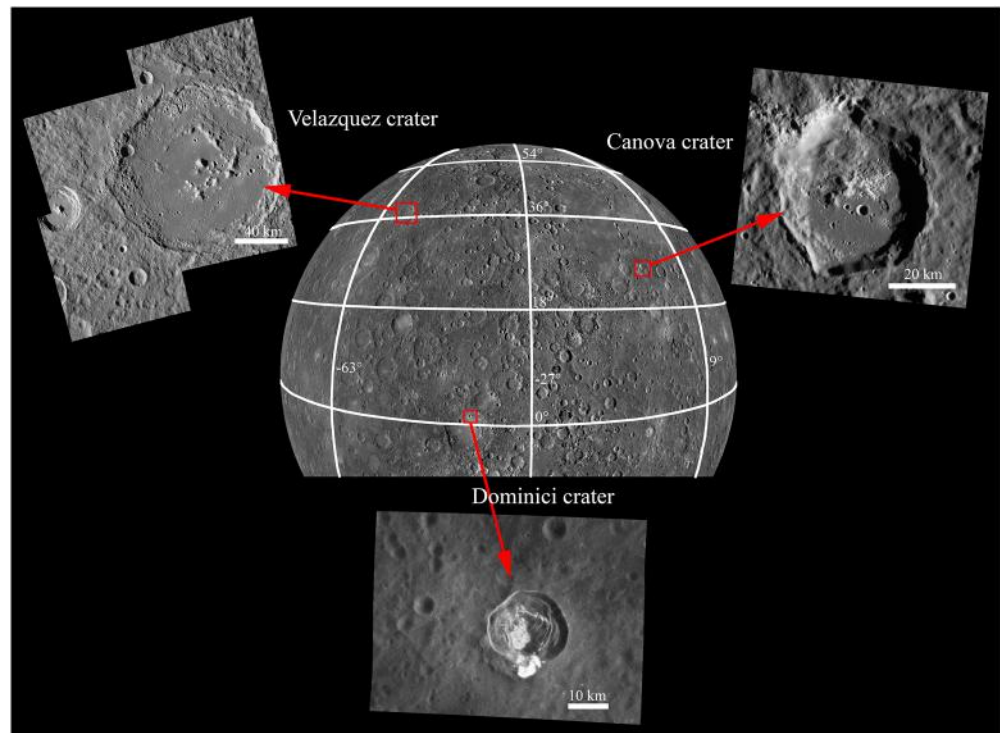


Figure 1. The craters analyzed in this work and their location on Mercury. (top left) A mosaic of wide angle camera images (186 m/px resolution) showing the Velazquez crater (center latitude = 37.74°N , center longitude = 55.3°W) characterized by a hollow area concentrated on the top of the peak ring. (top right) The narrow angle camera (NAC) image (EN0220588954M, 60 m/px resolution) showing the Canova crater (center latitude = 25.62°N , center longitude = 3.75°W) with hollows located on the floor and in correspondence of the ejecta of the crater. (bottom) The mosaic of NAC images (50-m/px resolution) showing Dominici crater (center latitude = 1.38°N , center longitude = 36.5°W) displaying hollows both in the center and in the south crater wall/rim.

As shown in Thomas et al. (2014), Mercury is characterized by the presence of hollows scattered all over the surface; hence, the choice of these targets was based on the data set availability covering these craters. The Dominici crater was selected in order to test the plausibility of our spectral clustering method, since a direct comparison between our compositional results and the spectral detection reported by Vilas et al. (2016) can be made. The other two craters were chosen in the Victoria quadrangle because the global geological map is freely available (Galluzzi et al., 2016) and because the image data sets have both appropriate resolution and spectral coverage to discriminate hollows from the surroundings.

2.1. High-Resolution Geological Maps

The existing geological maps available for Mercury encompass areas characterized by hollows. However, these features were never mapped in detail before, either because they were yet unknown (see Spudis & Guest, 1988, and references therein), not distinguishable at all in low-scale global products (e.g., Prockter, 2016), or marked just as surficial patterns in regional-scale products (e.g., Galluzzi et al., 2016). Hence, high-scale geological maps are required in order to provide a full geological framework where hollows formed.

In order to map small features such as hollows, we needed image frames provided by the MESSENGER MDIS/NAC instrument at a pixel scale of a few tens of meters or better. We processed NAC single frames or multiframe mosaics with U.S. Geological Survey (USGS) ISIS3 software. However, given the small spatial coverage of such frames, several projection mismatches between the mosaics were found. To avoid this issue, we kept the map-projected Basemap Data Record (~ 166 m/pixel) as a reference basemap and georeferenced the self-produced mosaics onto it to minimize feature location uncertainties. The USGS stereo-derived digital terrain model (v2, Becker et al., 2016) was used for a thorough interpretation of the surrounding surface morphology, although its resolution (665 m/pixel) was not compatible with the used NAC mosaics resolution.

We used European Space Research Institute ArcGIS software to perform the geological mapping, and we followed the USGS digital cartographic standard for map symbolization in order to provide an exhaustive cartographic product (https://ngmdb.usgs.gov/fgdc_gds/geolsymstd.php). We used an average mapping scale of 1:100,000, which was based on the available NAC resolution that ranged between 15 and 60 m/pixel.

The NAC images provide monochrome information about the surface; thus, our cartographic interpretation is mainly based on morphology and albedo.

All analyzed hollows are located within impact craters and impact crater materials. Therefore, we mapped these materials by following standard morphological criteria that permitted us to distinguish the crater floor, rim, proximal, and distal ejecta, along with their associated talus deposits. Hollow units were distinguished into three main categories mainly driven by the depression size: isolated hollows, hollow clusters, and hollow fields. Isolated hollows (*hi*) are represented by single depressions tens or a few hundred meters large. Hollow clusters (*hc*) are wider depressions, whose borders are often linked together forming irregular sunken areas hundreds of meters to a few kilometers in width. The hollow field *sensu stricto* (*hf*) unit was only attributed to extensive and very bright clusters of hollows, tens of kilometers large; in these cases isolated hollows are generally undistinguishable. All hollows units are very easy to recognize due to their high-reflectance values, which can be enhanced by applying a gamma correction to the images that helps bringing out details on their borders and floors (see Figure S1 in the supporting information). A fourth type of terrain associated with hollows was mapped as a surficial unit and called *ht*, hollowed terrain. This unit indicates areas of high albedo surrounding hollows that could be related to the hollow halo or to scattered sparse hollows, too small to be individually mapped. The main difference between the former hollows units and *ht* is that the latter usually disappears when decreasing the gamma value. For the Dominici crater's case the available NAC resolution was lower with respect to the other craters; therefore, it was not possible to distinguish whether some small bright areas were actually hollowed. For this reason we decided here to make use of the more generic unit "bright material" in the mapping nomenclature.

The three craters under study were mapped following the above-mentioned criteria, each of them showing different hollow characteristics as described below.

2.1.1. Dominici Crater

Dominici is a simple crater with a diameter of 20 km (Figure 2). It shows a sharp rim and a fresh morphology, both suggesting a young age. This is further confirmed by its well preserved continuous proximal ejecta (*epD*) blanket that shows the characteristic hummocky surface with a maximum extension of about 20 km from the crater rim. The fresh morphology coupled with the presence of rayed bright ejecta suggests that Dominici belongs to the Kuiperian time-stratigraphy system (Spudis & Guest, 1988). The wall of the crater shows several terraces, of different size, that alternate to steep scarps. In the geological map (Figure 2), the terrace margins have been outlined. A very narrow ribbon of crater wall is exposed, and it has been named as crater rim unit (*crD*, Figure 2). Indeed, the great part of terraces and scarps were covered by wall smooth taluses (*tws*, Figure 2). We classify as "talus" the gravitational deposits that are uniformly distributed along the foot of the scarps and show no defined source of origin. Although the detailed texture of the deposits is below the resolution of the available NAC images, the smooth appearance of their surface suggests that they are deposits of fine material. Locally, portions of crater rim appear to be head scarps of talus cones (*tc*, Figure 2), which are gravitational fine deposits with a clear source of origin. The areas not covered by taluses or talus cones appear buried by material showing a rough surface texture, and, for this reason, they have been classified as hummocky deposit (*hd*, Figure 2). These deposits are not uniformly distributed along the scarp's foot and they seem to predate taluses and talus cones. Therefore, they are interpreted to be fine material due to mass wasting of surrounding scarps and buried by subsequent talus and talus cones.

However, the main features characterizing the Dominici crater are the hollow fields (*hf*, Figure 2), mapped into the southern crater wall and in the center of the crater floor, respectively. Both fields are characterized by a high reflectance that does not allow the single hollows to be discriminated, although locally, some hollow margins have been identified. The two fields show different morphologies, as previously highlighted by Vilas et al. (2016), suggesting a different evolution.

Bright materials (*bm*, Figure 2) have been mapped in localized regions all over the crater wall. The two largest regions of bright material have been respectively distinguished over a talus, along a terrace

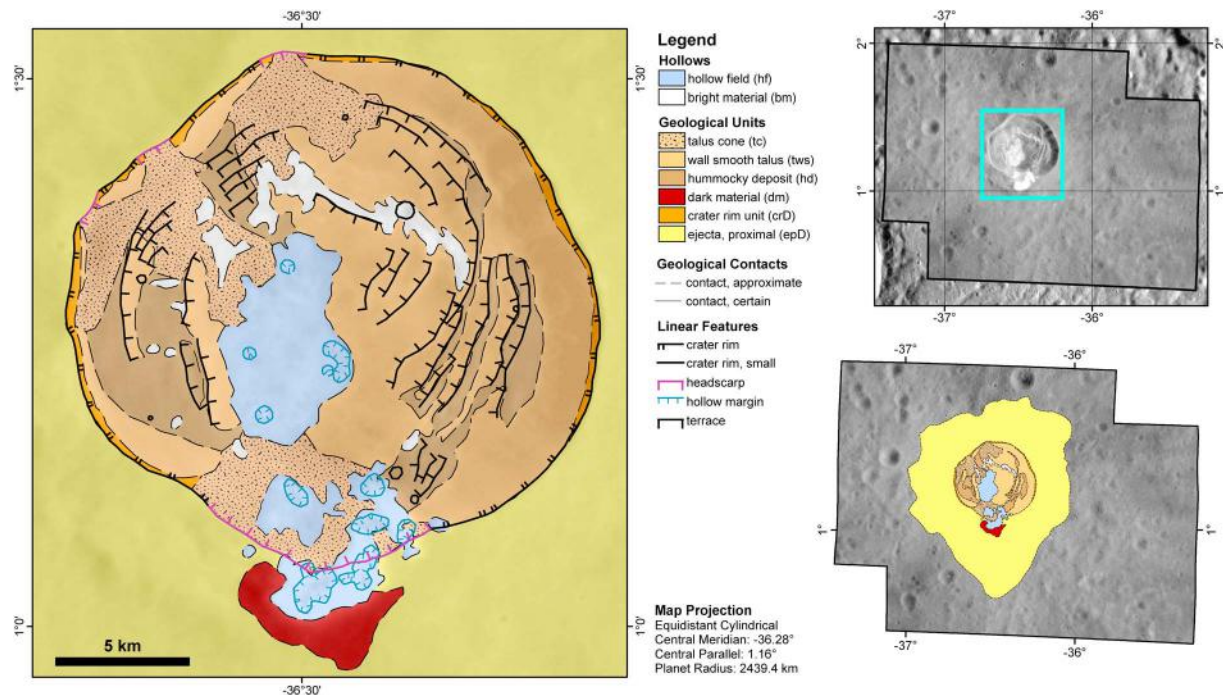


Figure 2. (left) High-resolution geological map of the Dominici crater (1.38°N, 36.5°W, 20-km diameter); (top right) overview of the Dominici crater on a monochrome basemap indicating the location of the detailed geological map (cyan box) and the high-resolution narrow angle camera mosaic coverage (black boundary); (bottom right) larger scale simplified geological map of the Dominici crater within the high-resolution mosaic boundary (geological units and contacts only). Hollows are here identified in the crater center and at the south wall/rim as outlined by the map.

margin in the northern part of the crater wall, and in the correspondence of a talus cone, in the northwest part of the crater wall.

The other bright regions are very limited in area and are mainly scattered in the western and southern parts of the crater wall, again over taluses or hummocky material. The resolution of the basemap (50 m/px) did not allow us to clearly detect the morphologies of these regions, in particular no depressions have been clearly distinguished. It is likely that these high reflectance areas represent bright deposits associated with very small hollows formed in a hollow-forming layer that outcrops along the terrace edges. Finally, also a dark region (*dm*, Figure 2) has been mapped on the south of Dominici crater, in the near rim ejecta and in proximity of the wall hollow field.

2.1.2. Canova Crater

The Canova 25-km sized crater (UC1, Figure 3) is located at 25.62°N, 3.75°W in a densely cratered intercrater plains area of the Victoria quadrangle (Galluzzi et al., 2016) in the vicinity of two other craters with prominent hollows: de Graft (Blewett et al., 2013, 2016) and Kyosai. It is emplaced on top of the northern rim of a larger crater with a diameter of 90 km (UC2). Its proximal ejecta (*epU1*, Figure 3) are visible only on the southern and eastern half of the rim, while the distal ejecta (*edU1*, Figure 3) fully cover the surrounding terrain leaving exposed the prominent morphology of UC2 central peak (*cpU2*, Figure 3) to the south. Impact melt from UC1 appears to have ponded in a small area just north of the UC2 central peak (see *mp*, Figure 3). The UC1 rim unit (i.e., not ejected material, see *crU1*, Figure 3) was mapped where the rim looks more prominent and has a sharper morphology with respect to the surrounding material. Despite of its small size, UC1 is a complex crater with a central peak; its offset position and the asymmetry of the crater's distal ejecta (less developed to the west) may imply a SE to NW impact direction. NAC images with resolution ranging from 30 to 60 m/px were used to cover this area in order to perform the mapping.

The hollows found within UC1 are located on the northern part of the floor spreading outward to the northwest beyond the rim, where no proximal ejecta are observed. The overall elongation of the hollow units is ESE-WNW, aligned with the asymmetry of the crater materials. Isolated hollows and cluster of hollows are found scattered within this elongated area highlighted by a bright *ht* halo. Some smooth talus deposits (*tws*, Figure 3) interrupt the continuity of the *ht*, hinting to a gravitational process that

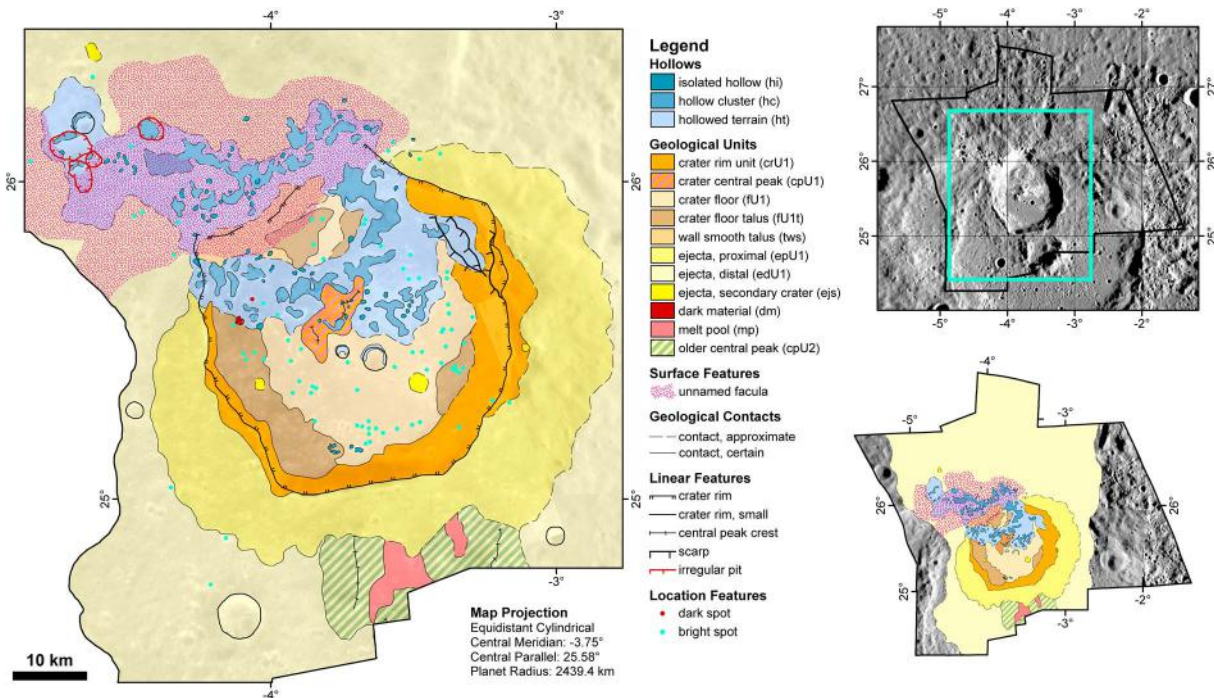


Figure 3. (left) High-resolution geological map of the Canova crater (25.62°N, 3.75°W, 25-km diameter), which is emplaced on top of the northern rim of a larger crater with a diameter of 90 km; (top right) overview of the Canova crater on a monochrome basemap indicating the location of the detailed geological map (cyan box) and the high-resolution narrow angle camera mosaic coverage (black boundary); (bottom right) larger scale simplified geological map of the Canova crater within the high-resolution mosaic boundary (geological units and contacts only). As outlined by the map, hollows are here identified outside the crater rim and in the northern part of the crater center (these crater floor hollows are the ones that are studied in detailed in this work).

happened during or after the formation of hollows that appear blurred, darkened, or lost in this area. Several secondary craters on UC1 floor are present, sometimes exposing fresh material on their rims or ejecta with a brightness comparable to the hollows' one. The northwestern part of the crater is characterized by an unnamed *facula* (i.e., a bright spot, usually associated to pyroclastic deposits on Mercury, Kerber et al., 2011), whose presence is subtle in the NAC mosaics, but it visible in most of global basemaps, and mainly on the low resolution principal component basemap. Such features are not visible on monochrome mosaics, but we marked its location with an overlying pattern to stress the fact that most *hc* in this area are on top of the *facula* (i.e., younger).

2.1.3. Velazquez Protobasin

Velazquez is a 125-km-sized crater located at 37.74°N, 55.3°W among a densely cratered intercrater plains region of the Victoria quadrangle, partly fading into a moderately cratered intermediate plains area (Galluzzi et al., 2016). Velazquez was classified as a protobasin by Baker et al. (2011) due to the presence of both a peak ring and a central peak. It presents rather symmetrical ejecta with a pool of ejected impact melt to the northwest (Galluzzi et al., 2016); however, hollows are concentrated just on the central part of the floor, as shown by the geologic map close up in Figure 4. A total of 52 useful NAC images were found to cover this area with a resolution ranging from 16 to 27 m/pixel. The central peak and peak ring rise out of a rather smooth floor moderately covered by smaller craters, whose ejecta are not as bright as those observed in UC1. The central peak and peak ring nearby the *ht* unit are rather bright when hit by sunlight (pVb), probably because, similarly to that unit, they encompass very small hollows. Other peaks far from the *ht* unit where mapped as crater peak (cpV) because they are not as bright as pVb in the used NAC mosaics.

Hollows are located mostly on top and around the southern part of the peak ring, which does not perfectly develop concentrically with respect to the crater floor. There are no hollows on the actual central peak just north of the *ht*, although its albedo is very bright with respect to the surroundings. Hollow clusters with very irregular borders are scarcely developed, while several isolated hollows are found scattered within the *ht*, especially on top of the peaks, as already reported by Blewett et al. (2013).

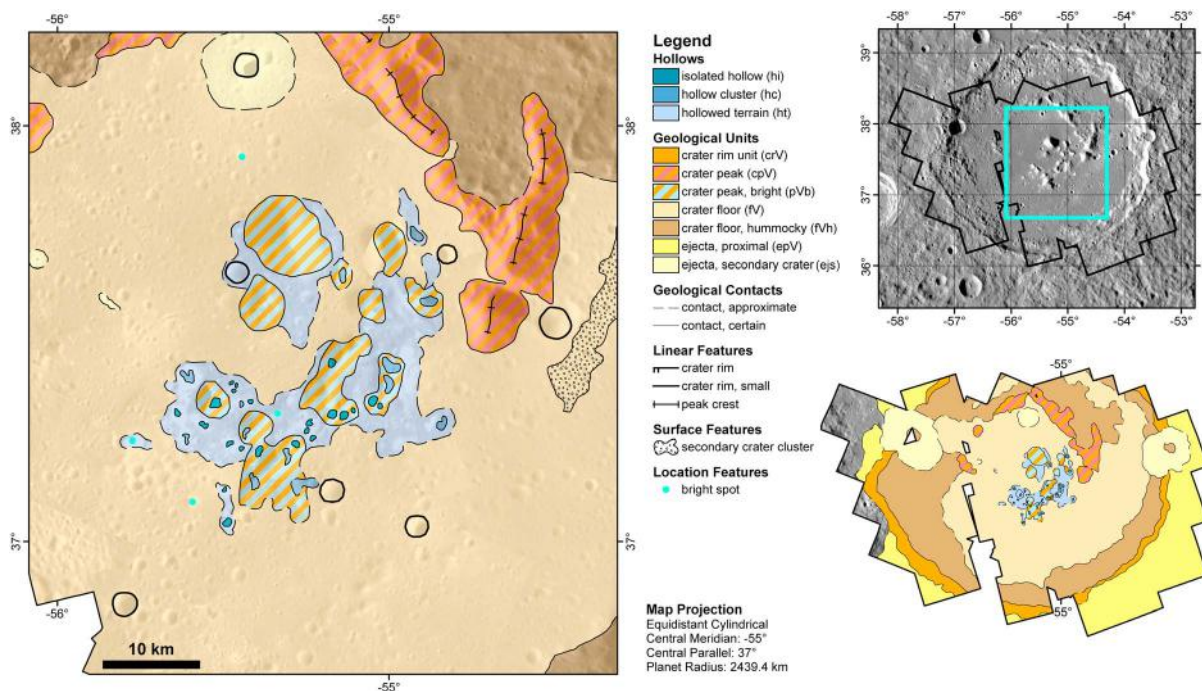


Figure 4. (left) High-resolution geological map of the Velazquez crater (37.74°N, 55.3°W, 125 km diameter); (top right) overview of the Velazquez crater on a monochrome basemap indicating the location of the detailed geological map (cyan box) and the high-resolution narrow angle camera mosaic coverage (black boundary); (bottom right) larger scale simplified geological map of the Velazquez crater within the high-resolution mosaic boundary (geological units and contacts only). Hollows are here identified on the top of the peak ring, as outlined by the map.

2.2. Spectral Clustering

We applied a spectral clustering technique on the craters encompassing hollows using multispectral WAC data sets. First, we applied radiometric and photometric correction to all images using the ISIS3 image processing package of the USGS. For each crater the following WAC data sets were used:

- Dominici crater: data set with a scale of 935 m/px through eight filters (0.433, 0.479, 0.558, 0.628, 0.748, 0.828, 0.898, and 0.996 μm);
- Canova crater: data set with a scale of 265 m/px through 11 filters (0.433, 0.479, 0.558, 0.628, 0.698, 0.748, 0.828, 0.898, 0.947, 0.996, and 1.012 μm); and
- Velazquez crater: data set with a scale of 260 m/px through 11 filters (0.433, 0.479, 0.558, 0.628, 0.698, 0.748, 0.828, 0.898, 0.947, 0.996, and 1.012 μm).

The images have been photometrically corrected with Hapke methods, using parameters derived in Domingue et al. (2015), that is, incidence angle of 30°, emission angle of 0°, and phase angle of 30°. On the unnormalized photometrically corrected data set we applied a statistical clustering over the entire data set based on K-means algorithm (Marzo et al., 2006). The method was developed and evaluated by Marzo et al. (2006, 2008, 2009) and makes use of the Calinski-Harabasz criterion (Calinski & Harabasz, 1974) to find the intrinsic number of clusters, making the process unsupervised. A natural number of ten clusters was identified within each crater under study and its closest surroundings (Figures 5–7). We applied the clustering on the overall Dominici crater, while for the Canova and the Velazquez cases we selected a small area of the craters. This was done in order to directly focus and highlight the hollow behavior in all three cases. We point out that the equal finding of 10 clusters for each crater is a random result because the process is unsupervised. Each resulting cluster is characterized by an average spectrum and its associated variability (see the Tables S1, S2, and S3 in the supporting information for the corresponding average I/F and associated sigma values). In addition, the relative geographic information of each spectrum is maintained in the process, and the resulting clusters can be correlated with high-resolution geological maps previously described. This approach has been already applied for compositional interpretations of different solar system objects, for example, Mars, Iapetus, and Phobos (Dalle Ore et al., 2012; Marzo et al., 2006, 2008; Pajola et al., 2018;

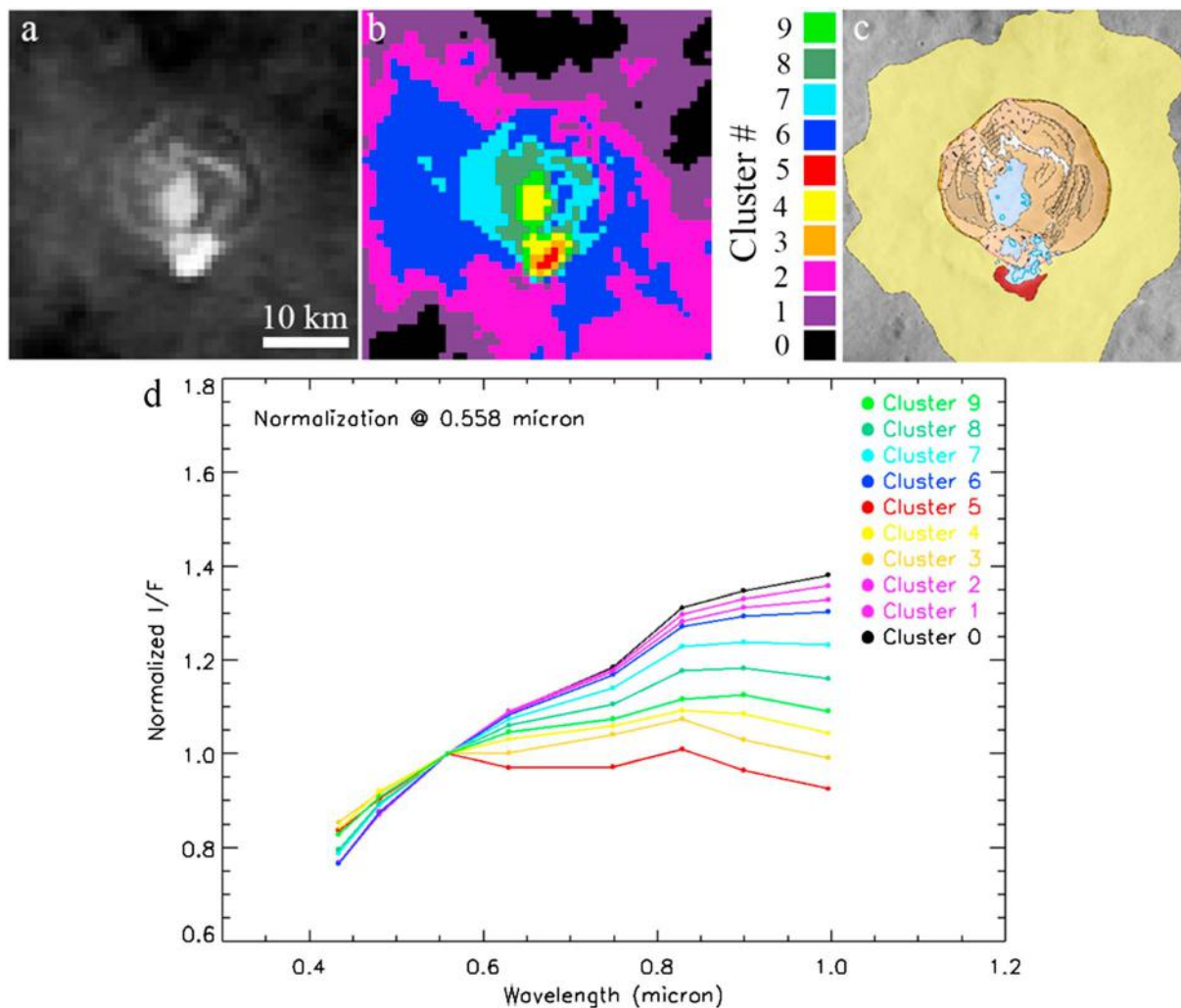


Figure 5. (a) The wide angle camera reference image (EW0210848973D) for Dominici crater, (b) the relative 10 clusters identified in the Mercury Dual Imaging System data sets after the application of the k-mean algorithm, and (d) the average spectra normalized to a value of 1.0 at 0.558 μm . We refer to the supporting information to report the average I/F value for the clusters and its associated variability. The colors of the spectra refer to (b). (c) High detailed geomorphological map of the Dominici crater (see Figure 2 for the legend). The comparison between the clusters location and the geomorphological units reveals a strong correlation between the two data; in particular the hollows are represented by clusters 3 and 4 and mainly cluster 5.

Pinilla-Alonso et al., 2011). This technique is agnostic of the physical meaning of the clusters; hence, scientific interpretation is required as part of the subsequent evaluation of the results.

3. Results and Discussion

3.1. Comparison Between Geomorphological Maps and Spectral Clusters

The exploitation of the clustering technique provides the possibility to correlate well-defined geomorphological settings together with their spectral properties. Indeed, the spectral clusters exhibit a spatially coherent distribution, highlighting a clear correlation with the units indicated by detailed geomorphological maps. Moreover, the characteristics of the 10 clusters identified on each crater suggest a different composition based on differences outlined in spectrum behavior. The main results of such comparison are outlined in Figures 5–7 for the Dominici, Canova, and Velazquez craters, respectively.

As shown in Figure 5 the clustering technique applied on the Dominici image subset (50 \times 50 pixel size) spectrally separates the crater surrounding terrains (clusters 0, 1, 2, and 6), from its interior, which is characterized by taluses (clusters 7 and 8). The two hollow fields, which have been identified in Figure 2, are clustered in three areas (clusters 3–5) with cluster 5 located in correspondence of the brighter portion of the southern

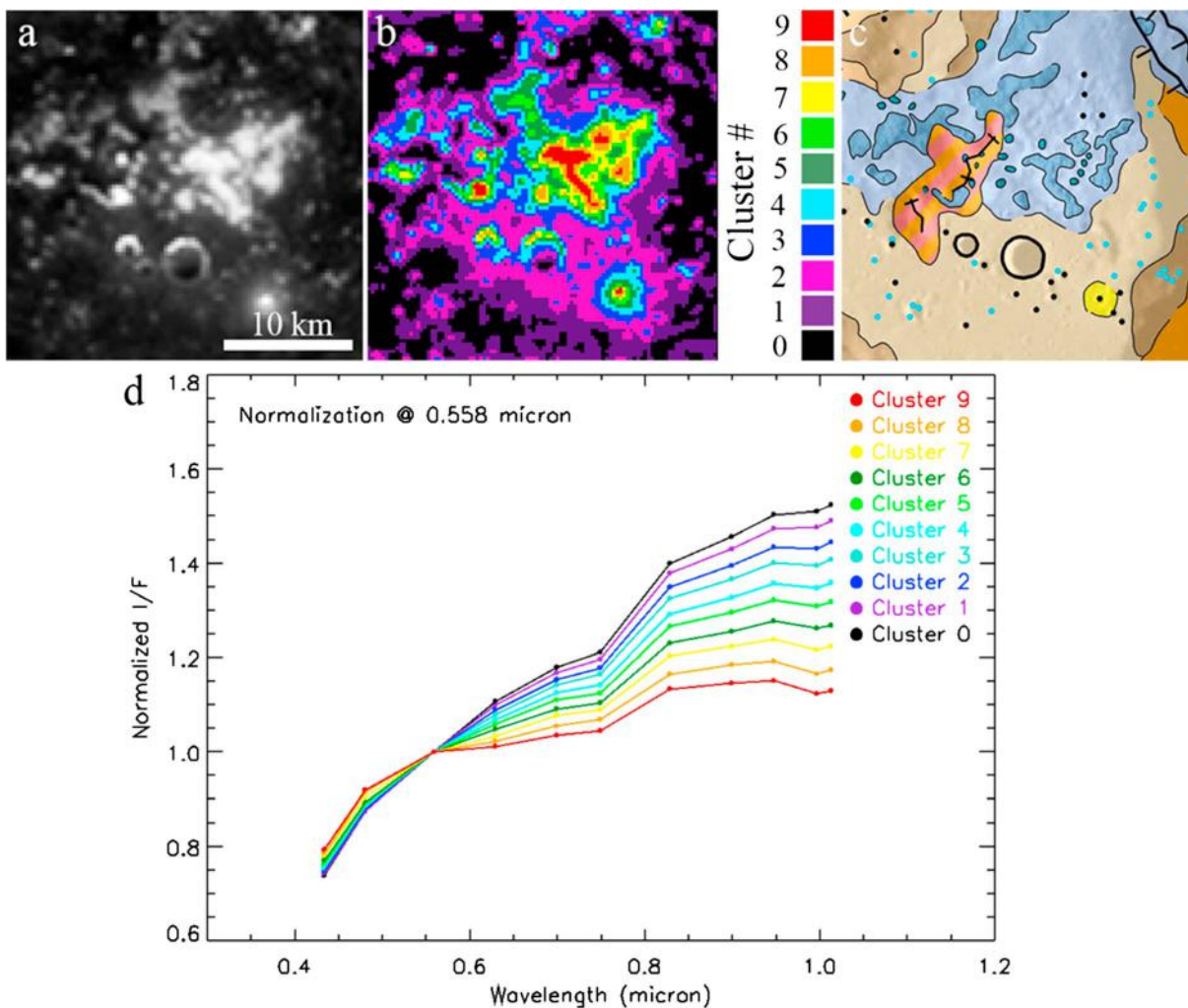


Figure 6. (a) The wide angle camera reference images (EW1017269227D) for Canova crater, (b) the relative 10 clusters identified in the Mercury Dual Imaging System data sets after the application of the k-mean algorithm, and (d) the average spectra normalized to a value of 1.0 at 0.558 μm . We refer to the supporting information to report the average I/F value for the clusters and its associated variability. The colors of the spectra refer to (b). (c) Close up of the high detailed geomorphological map of the Canova crater showing hollows (see Figure 3 for the legend). The comparison between the clusters location and the geomorphological units reveals a strong correlation between the two data, in particular the hollows are represented by clusters 7, 8, and mainly 9.

hollow field. Hollows are clearly separated by the spectral clustering technique from the rest of the inner crater talus terrains (clusters 7 and 8) and from their edges (cluster 9). Clusters 0, 1, 2, and 6 typically present a red slope in the visible and near-infrared with a possible weak absorption band centered at 0.748 μm . Clusters 7–9 show almost no absorption between 0.558 and 0.828 μm and seem to be representative of a possible “spectral transition” between the surrounding terrain and the hollows groups. Cluster 5 is located on the brightest part of the south wall/rim of Dominici crater; it shows the most peculiar spectrum, with a wide absorption band between 0.558 and 0.828 μm . Moreover, its spectrum is characterized by a hint of absorption toward the IR. Similarly, clusters 3 and 4 show the same absorption band, but less pronounced.

The cluster 5 detection is consistent with the one reported by Vilas et al. (2016) that found similar absorption in the crater center, here spatially correlated to cluster 4. Clusters 4 and 3 are also located on the south wall/rim of the crater together with cluster 5. Nevertheless, from the geological map in Figure 2, it is shown that the hollows in the south wall/rim are placed into two distinct groups: the eastern and the western ones. The eastern ones include depressions with sharp margins and fresh morphology. A talus cone originated from the crater wall had probably revealed these hollows (Vilas et al., 2016); likely, this field is also lightly eroded. Instead, the western group of hollows on the crater walls appears partially buried by the talus

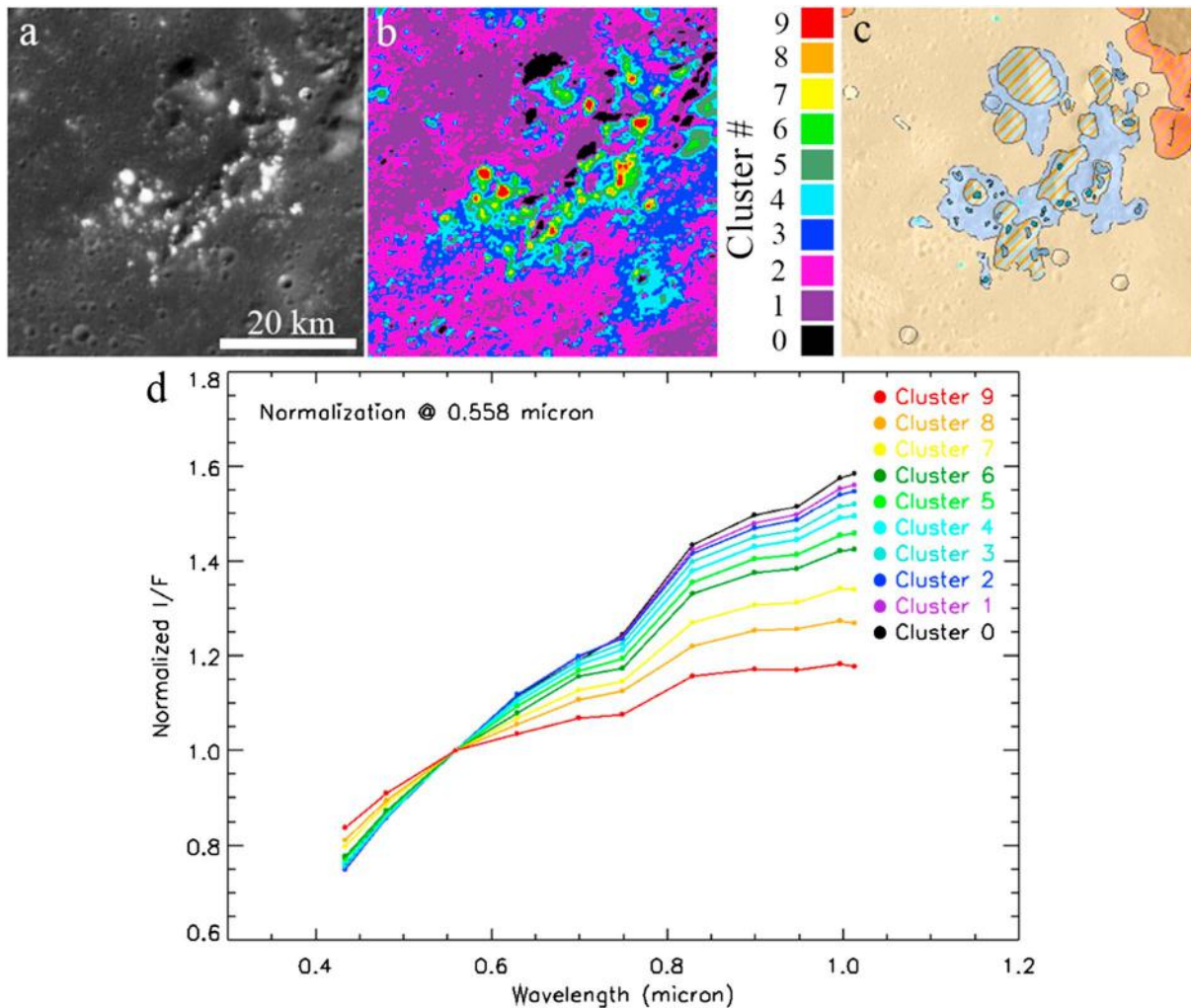


Figure 7. (a) The wide angle camera reference images (EW1020781879D) for Velazquez crater, (b) the relative 10 clusters identified in the Mercury Dual Imaging System data sets after the application of the k-mean algorithm, and (d) the average spectra normalized to a value of 1.0 at 0.558 μm . We refer to the supporting information to report the average I/F value for the clusters and its associated variability. The colors of the spectra refer to (b). (c) Close up of the high detailed geomorphological map of the Velazquez crater (see Figure 4 for the legend). The comparison between the clusters location and the geomorphological units reveals a strong correlation between the two data; in particular the hollows are represented by clusters 7, 8, and mainly 9.

cone. It is worth noting that although the hollowed area is buried by mass wasting deposits, its brightness is still clearly discernible. On the other hand, the hollow field into the center of the crater floor is more extended, covering a surface of about 28 km^2 . However, the depressions into this field are very shallow and their margins are highly eroded and generally difficult to distinguish. Moreover, the field shows a lower reflectance than the one of the wall field (Figure 2). Such evidence suggests that whether the field has been affected by erosive processes for a longer period than the crater wall ones, or it is at a higher stage of formation, in accordance with Vilas et al. (2016). This is coherent with the hollow discrimination outlined by our clusters: Cluster 5 can be associated with the fresher wall hollows, while clusters 3 and 4 can be associated with the hollows interested by intermediate and high erosion processes, respectively. Therefore, for the subsequent spectral interpretation, we consider cluster 5 as the one representative of hollow spectrum in the Dominici case since the absorption band is more pronounced with respect to clusters 3 and 4.

Figure 6 shows the results from the application of the clustering technique on the Canova crater. The spectral clustering has been performed on a small area of the WAC data set (100 \times 100 pixel size) underlying the region presenting hollows on the floor of the crater (Figure 6). In this case, the absorption band between 0.558 and 0.828 μm reappears, being again coupled with the location of hollows, as outlined by the

comparison with the geomorphological map. Clusters 7–9 show the most peculiar spectra. In particular cluster 9 fits the location of hollows both on the crater's floor and on the top of the central peak, as shown by the close up of the geological map in Figure 6. Clusters 0–3 correspond to the floor of the crater, while clusters 4–6 show intermediate spectra between the hollows and the crater floor ones, probably representing an intermediate unit (defined as hollowed terrain in the geomorphological map). The presence of hollows (mainly identified by cluster 9) both on the crater floor and on ejecta suggests that the mechanism forming hollows has triggered material at shallow depth. Even if small hollows are found on the central peak, the absence of these peculiar features in the crater underneath the Canova one confirms that hollow-forming material may be rather shallow.

The analysis of the Velazquez crater (image subset of 200×200 pixel size) is reported in Figure 7. For this specific case, the hollows are located on the top and around the southern part of its peak ring. The results obtained for Velazquez are similar to the previous two case studies. In particular, cluster 7, 8, and mainly 9 show again the absorption band between 0.558 and $0.828 \mu\text{m}$ in correspondence to the hollow location, as outlined by the units mapped in the geological map. Clusters 4–6 are found surrounding the hollow location and in correspondence to the central peak and peak ring, when compared to the units mapped in the geological map. Hence, they might be considered as a transitional behavior between hollows spectra and crater's floor spectra, which are identified by clusters 0–3. The hollow features (mainly identified by cluster 9) are concentrated on the crater peak ring, implying that the mechanism forming hollows has triggered material located at larger depths compared to the Canova crater case. Indeed, Velazquez exhibits a peak ring structure, which is commonly the part of a crater that is exhumed from the greatest depth.

As reported from the overall analysis characterizing these craters, we point out that there is a good correlation between the identified spectral clusters and the well-defined geomorphological units (as highlighted in Figures S2, S3, and S4). In particular, the hollows are uniquely identified by a well-defined spectrum in all craters. Clusters 5 in Dominici crater and cluster 9 for the Canova and Velazquez craters show the most peculiar spectra representing hollows with a well-defined absorption band between 0.558 and $0.828 \mu\text{m}$, which has different shape depending on the crater under consideration. In addition, there is a possible hint of absorption toward $1 \mu\text{m}$, clearly visible for the Dominici case. The difference between the shape of the absorption band between 0.558 and $0.828 \mu\text{m}$ can be associated to the data sets' filters used in the analysis. Indeed, the Canova and Velazquez cases present one more filter inside the band between 0.558 and $0.828 \mu\text{m}$ with respect to the Dominici case: This may result in the occurrence of two absorption peaks inside the band, especially for the Canova case. The different spectral behavior of hollows in our case studies can also be attributed to the different geomorphological setting in which hollows have formed. As stated above, we expect that the mechanism forming hollows located in Velazquez crater's central peak involves material that originated at large depth in the planets' crust, while for Canova the material forming hollows comes from a shallower depth. In the following analysis, these specific spectra are compared with possible spectra analogues to infer the composition of hollow features.

3.2. Spectral Matching and Mineralogical Implications

The morphology of hollows suggests that the most probable formation scenario is the one proposed by Blewett et al. (2013, 2016). That is, first a proportion of the parent material is volatilized to form hollows, leaving behind a lag that ultimately prevents the further deepening, and then the high relief hollow margins continue to recede, widening the hollow. Ca and Mg are the most common cited candidates for the relatively volatile material (Blewett et al., 2011; Helbert et al., 2013) based on the high concentration of sulfur detected at Mercury's surface (Evans et al., 2012; Nittler et al., 2011) as well as on the correlation between sulfur, calcium, and magnesium abundance in heavily cratered terrains (Weider et al., 2015). Indeed, Vilas et al. (2016) attributed to CaS and MgS the absorption band found in the Dominici crater, even if thermal cycling of these candidate minerals suggests that the extreme heating during a Mercury day could generally weaken spectral absorption features over extended time periods (e.g., Helbert et al., 2013). However, Vilas et al. (2016) proposed that exposed sulfides from the subsurface could remain unheated because the mechanism forming hollows creates porosity in the material, hence reducing the heat propagation.

In addition to CaS and MgS, the MnS sulfide retains an absorption band centered near $0.650 \mu\text{m}$ after heating cycles (Helbert et al., 2013), but the upper limit abundance on the Mercury surface is relatively low as reported by MESSENGER measurements (0.49 wt%, Peplowski et al., 2012). Our case studies are

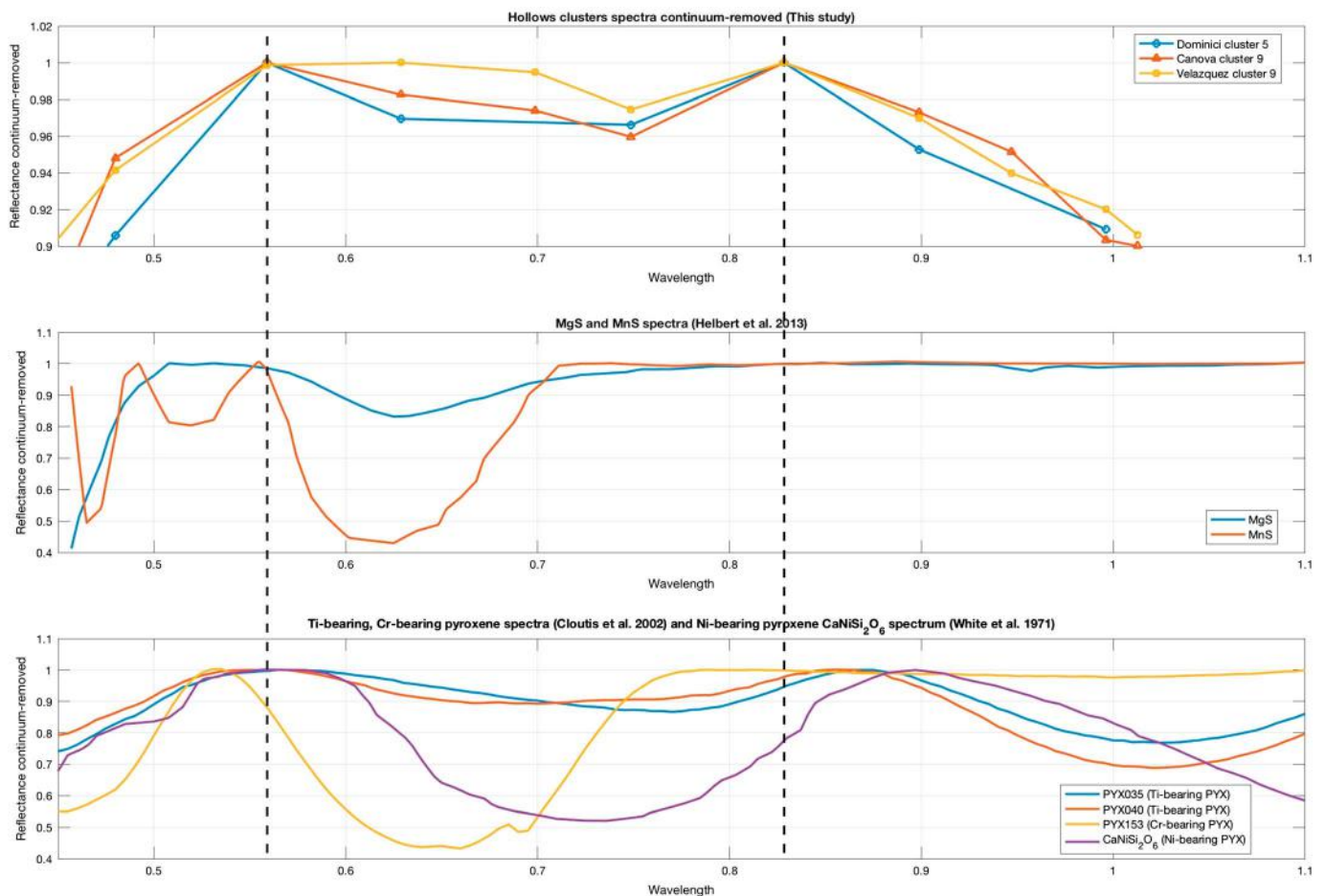


Figure 8. Comparison between continuum removed hollow spectra obtained in this work (cluster 5 for Dominici, cluster 9 for Canova and Velazquez) and identified end members. (top) The continuum removed hollow spectra; (middle) the continuum removed MgS and MnS spectra reported in Helbert et al. (2013), which are already cited candidates for hollow composition in literature. (bottom) The continuum removed pyroxene (PYX) spectra identified in this work (Cloutis, 2002; White et al., 1971) that show a wide absorption band between 0.558 and 0.828 μm (typical of hollows spectra shown on top) and an absorption toward 1 μm . The absorbance Ni-bearing pyroxene spectrum reported in White et al. (1971) is here converted in reflectance units through the formula $\text{Abs} = \log(1/\text{ref})$ for a better spectrum comparison. From the comparison, we infer that hollow spectra can be the results of the mixing of different material (pyroxenes and sulfides) that contribute in different percentages to the absorption observed.

not strictly correlated with any element abundances maps reported by X-ray measurements (our craters are located nearby medium concentration of Mg/Si, Weider et al., 2015); hence, we do not expect strong sulfides absorption bands, even if we cannot exclude that sulfides can be present at those locations. Moreover, the resolution of X-ray measurements is too low (order of hundreds of kilometers) when compared to our image data set (order of hundreds of meters). This implies that we can locally find elements whose total abundances reported by X-ray measurements are instead low or not present. Following these considerations we explore the possibility to suggest other minerals, besides sulfides, in order to fit the hollow spectral behavior. This is also supported by the spectral trend of CaS, MnS, MgS (Figure 8) that present an absorption feature centered near 0.650 μm , while they do not have wide absorption from 0.558 to 0.828 μm (this is the typical behavior of our hollows spectra). We point out that the wide absorption between 0.558 and 0.828 μm found in our MDIS spectra has never been observed in Mercury Atmospheric and Surface Composition Spectrometer-Visible and Infrared Spectrograph (McClintock & Lankton, 2007) spectra (e.g., Izenberg et al., 2014; Murchie et al., 2015). This could be explained by the larger VIRS footprint with respect to the field of hollows analyzed in our work. In addition to this wide absorption, the hint of absorption toward 1 μm found in our spectra cannot be simply explained by sulfides. For this reason, we introduce other minerals that could contribute to the absorption identified in our results.

We therefore consider silicate minerals since it is accepted that hollows have formed in crust-rock forming material and it is plausible that part of it characterizes what we are observing (Namur & Charlier, 2017; Vander Kaaden & McCubbin, 2015). Indeed, mineralogical variability in silicates of Mercury's crust was investigated finding a close relation to the geochemical terrains (Namur & Charlier, 2017). Through multiple comparisons, we identified different end-members that could be responsible for the observed absorption of hollows, in association (or not) with sulfides such as pyroxenes presenting transitional elements other than Fe^{2+} . The presence of pyroxenes containing transitional elements (Cr, Mn, Ti, Ni, etc.) is supported by X-ray measurements. Indeed, the reported global average of Cr/Si and Ti/Si abundances of 0.005 and 0.011, respectively (Nittler et al., 2011; Weider et al., 2014, 2015), justifies the presence of such elements on the surface of the planet. In addition, Cr, Ti, and other transitional elements are considered by Peplowski et al. (2015) to support the high value of macroscopic neutron absorption cross section found in some regions. Hence, in our analysis, we consider the following minerals presented in Figure 8. The first one is an ureyite (Na-Cr pyroxene, named PYX153, PP-EAC-090 in RELAB catalogue, Cloutis, 2002) presenting a visible band with maximum absorption near $0.650 \mu\text{m}$ but broader than the one presented by the sulfides spectra. In addition, even if little iron content is present in Cr-bearing pyroxenes (Cloutis, 2002), the absorption around $1 \mu\text{m}$ can occur, hence justifying the detected absorption hint (see PYX018 and PYX170 spectra in Figure 4 in Cloutis, 2002). Moreover, we consider Ti-bearing pyroxenes (PYX035 and PYX040, PP-EAC-018 and PP-EAC-029 in RELAB catalogue, respectively) that show a wide absorption located in the spectral region interested by our hollow fields. In these samples, the presence of FeO is not neglected and it is related to the absorption at $1 \mu\text{m}$ with FeO. Other transitional elements can be found in pyroxene minerals that contribute to diagnostic absorption feature, as the spectrum reported related to a Ni-bearing pyroxene in Figure 8 (White et al., 1971). Ni is an element often found in meteorites, including in phases such as metal, sulfides, and rarely in silicates, and it has been associated to terrestrial olivine mafic minerals related to primitive basalts or Mg-enriched lava (e.g., Nishizawa et al., 2017). In addition, on Mercury we cannot rule out that Ni-bearing pyroxenes may be crystallized before the removal of Ni in the core magma and therefore be present in the crust-rock forming material. As shown in Figure 8, Ni-bearing pyroxene presents a wide band between 0.57 and $0.89 \mu\text{m}$, which fits with the absorption found in our spectra, in particular for the Dominici case; moreover, Ni^{2+} could be responsible also for the crystal field absorption around $1 \mu\text{m}$.

By comparing our spectra with the end members reported in Figure 8, we suggest that the composition of hollows is due to the presence of a mixture of different minerals (sulfides and silicates with different relative abundances) that may contribute to the absorption found in our spectra. These findings must consider the limitation of the MDIS WAC calibration reported in Denevi et al. (2018), suggesting caution in interpreting features in MDIS spectra found in individual WAC data sets. Indeed, temporal variations observed in MDIS responsivity result in the presence of spurious spectral features in WAC color sets. All such evidences suggest that the spectral artifacts are constant within a given multispectral image set. Hence, as reported by Denevi et al. (2018), future refinement and improvements to the calibration of the WAC data set must be performed for spectral studies that make use of the individual WAC color sets.

4. Conclusions

The NASA MESSENGER spacecraft has observed for the first time unusual morphological features on the surface of Mercury named hollows. Since the nature and the characterization of hollows are still open questions, we here analyzed in greater detail the nature of hollows both from a geomorphological and a compositional perspective. We performed detailed geological mapping of three different craters hosting hollows (Dominici, Canova, and Velazquez), making use of NAC high-resolution images, in order to fully characterize the geological framework where these features formed. Moreover, we applied a spectral clustering technique based on a K-mean algorithm that allows us to separate in different clusters our studying areas. The results from the application of the spectral clustering showed a strong correlation with the geomorphological units identified in high-resolution geological maps highlighting the value of this methodology. Through the spectral clustering, we were able to extract the spectra characterizing hollows alone, in order to study their spectral character in greater detail. We found that in all cases, the hollows exhibit spectral similarities related to a wide absorption band between 0.558 and $0.828 \mu\text{m}$, whose shape is different depending on the case study, and a possible hint of absorption at $1 \mu\text{m}$.

Previous studies suggest that the composition of hollows is related to remnant material from a process that involves devolatilization; in particular Ca and Mg sulfides are the most commonly cited candidates for the relatively volatile constituent. However, from our results, we suggested that the sulfides alone cannot explain the hollow spectra. Hence, other minerals that could be responsible of the absorption found in hollow spectra have to be taken into consideration. In particular, we consider pyroxenes presenting transitional elements, like Cr, Ti, and Ni, as candidates for explaining the spectral properties of hollows. These pyroxenes have broad absorptions between 0.558 and 0.828 μm and also possess absorption near 1 μm , which may be present in the MDIS spectra of hollows.

We advance the hypothesis that the spectra characterizing hollows are the result of the mixing of different phases that contribute to the observed absorption. Therefore, hollow terrains are the expression of both the remnant material coming from a process that involve degassing and the bedrock-forming material in which they formed.

Acknowledgments

We gratefully acknowledge funding from the Italian Space Agency (ASI) under ASI-INAF agreement 2017-47-H.0. This work made use of the Integrated Software for Imagers and Spectrometers (ISIS), which is a product maintained by the U.S. Geological Survey Astrogeology Science Center. MESSENGER data are available through the NASA Planetary Data System. We gratefully acknowledge David T. Blewett and an anonymous reviewer for constructive comments that improved the quality of the manuscript.

References

- Baker, D. M. H., Head, J. W., Schon, S. C., Ernst, C. M., Prockter, L. M., Murchie, S. L., et al. (2011). The transition from complex crater to peak-ring basin on Mercury: New observations from MESSENGER flyby data and constraints on basin. *Planetary and Space Science*, 59(15), 1932–1948. <https://doi.org/10.1016/j.pss.2011.05.010>
- Becker, K. J., Robinson, M. S., Becker, T. L., Weller, L. A., Edmundson, K. L., Neumann, G. A., et al. (2016). First global digital elevation model of Mercury. In *Lunar and Planetary Science Conference* (Vol. 47, p. 2959).
- Blewett, D. T., Chabot, N. L., Denevi, B. W., Ernst, C. M., Head, J. W., Izenberg, N. R., et al. (2011). Hollows on Mercury: MESSENGER evidence for geologically recent volatile-related activity. *Science*, 333(6051), 1856–1859. <https://doi.org/10.1126/science.1211681>
- Blewett, D. T., Stadermann, A. C., Susorney, H. C., Ernst, C. M., Xiao, Z., Chabot, N. L., et al. (2016). Analysis of MESSENGER high-resolution images of Mercury's hollows and implications for hollow formation. *Journal of Geophysical Research: Planets*, 121, 1798–1813. <https://doi.org/10.1002/2016JE005070>
- Blewett, D. T., Vaughan, W. M., Xiao, Z., Chabot, N. L., Denevi, B. W., Ernst, C. M., et al. (2013). Mercury's hollows: Constraints on formation and composition from analysis of geological setting and spectral reflectance. *Journal of Geophysical Research: Planets*, 118, 1013–1032.
- Calinski, T., & Harabasz, J. (1974). A dendrite method for cluster analysis. *Communications in Statistics*, 3, 1–27.
- Cloutis, E. A. (2002). Pyroxene reflectance spectra: Minor absorption bands and effects of elemental substitutions. *Journal of Geophysical Research*, 107(E6), 5039. <https://doi.org/10.1029/2001JE001590>
- Dalle Ore, C. M., Cruikshank, D. P., & Clark, R. N. (2012). Infrared spectroscopic characterization of the low-albedo materials on Iapetus. *Icarus*, 221(2), 735–743. <https://doi.org/10.1016/j.icarus.2012.09.010>
- Denevi, B. W., Chabot, N. L., Murchie, S. L., Becker, K. J., Blewett, D. T., Domingue, D. L., et al. (2018). Calibration, projection, and final image products of MESSENGER's Mercury Dual Imaging System. *Space Science Reviews*, 214(1), 2. <https://doi.org/10.1007/s11214-017-0440-y>
- Denevi, B. W., Robinson, M. S., Solomon, S. C., Murchie, S. L., Blewett, D. T., Domingue, D. L., et al. (2009). The evolution of Mercury's crust: A global perspective from MESSENGER. *Science*, 324(5927), 613–618. <https://doi.org/10.1126/science.1172226>
- Domingue, D. L., Murchie, S. L., Denevi, B. W., Ernst, C. M., & Chabot, N. L. (2015). Mercury's global color mosaic: An update from MESSENGER's orbital observations. *Icarus*, 257, 477–488. <https://doi.org/10.1016/j.icarus.2014.11.027>
- Evans, L. G., Peplowski, P. N., Rhodes, E. A., Lawrence, D. J., McCoy, T. J., Nittler, L. R., et al. (2012). Major-element abundances on the surface of Mercury: Results from the MESSENGER gamma-ray spectrometer. *Journal of Geophysical Research*, 117, E00L07. <https://doi.org/10.1029/2012JE004178>
- Galluzzi, V., Guzzetta, L., Ferranti, L., Di Achille, G., Rothery, D. A., & Palumbo, P. (2016). Geology of the Victoria quadrangle (H02), Mercury. *Journal of Maps*, 12(sup1), 227–238. <https://doi.org/10.1080/17445647.2016.1193777>
- Gillis-Davis, J., van Niekerk, D., Scott, E., McCubbin, F. M., & Blewett, D. T. (2013). Impact darkening: A possible mechanism to explain why Mercury is spectrally dark and featureless. In AGU Fall Meeting Abstracts.
- Goldsten, J. O., Rhodes, E. A., Boynton, W. V., Feldman, W. C., Lawrence, D. J., Trombka, J. I., et al. (2007). The MESSENGER gamma-ray and neutron spectrometer. *Space Science Reviews*, 131(1–4), 339–391. <https://doi.org/10.1007/s11214-007-9262-7>
- Hawkins, S. E., Boldt, J. D., Darlington, E. H., Espiritu, R., Gold, R. E., Gotwols, B., et al. (2007). The Mercury Dual Imaging System on the MESSENGER spacecraft. *Space Science Reviews*, 131(1–4), 247–338. <https://doi.org/10.1007/s11214-007-9266-3>
- Helbert, J., Maturilli, A., & D'Amore, M. (2013). Visible and near-infrared reflectance spectra of thermally processed synthetic sulfides as a potential analog for the hollow forming materials on Mercury. *Earth and Planetary Science Letters*, 369–370, 233–238. <https://doi.org/10.1016/j.epsl.2013.03.045>
- Izenberg, N. R., Klima, R. L., Murchie, S. L., Blewett, D. T., Holsclaw, G. M., McClintock, W. E., et al. (2014). The low-iron, reduced surface of Mercury as seen in spectral reflectance by MESSENGER. *Icarus*, 228, 364–374. <https://doi.org/10.1016/j.icarus.2013.10.023>
- Kerber, L., Head, J. W. III, Blewett, D. T., Solomon, S. C., Wilson, L., Murchie, S. L., et al. (2011). The global distribution of pyroclastic deposits on Mercury: The view from MESSENGER flybys 1–3. *Planetary and Space Science*, 59(15), 1895–1909. <https://doi.org/10.1016/j.pss.2011.03.020>
- Klima, R. L., Denevi, B. W., Ernst, C. M., Murchie, S. L., & Peplowski, P. N. (2018). Global distribution and spectral properties of low-reflectance material on Mercury. *Geophysical Research Letters*, 45, 2945–2953. <https://doi.org/10.1002/2018GL077544>
- Lucey, P. G., & Riner, M. A. (2011). The optical effects of small iron particles that darken but do not redden: Evidence of intense space weathering on Mercury. *Icarus*, 212(2), 451–462. <https://doi.org/10.1016/j.icarus.2011.01.022>
- Marzo, G. A., Roush, T. L., Blanco, A., Fonti, S., & Orofino, V. (2006). Cluster analysis of planetary remote sensing spectral data. *Journal of Geophysical Research*, 111, E03002. <https://doi.org/10.1029/2005JE002532>
- Marzo, G. A., Roush, T. L., Blanco, A., Fonti, S., & Orofino, V. (2008). Statistical exploration and volume reduction of planetary remote sensing spectral data. *Journal of Geophysical Research*, 113, E12009. <https://doi.org/10.1029/2008JE003219>
- Marzo, G. A., Roush, T. L., & Hogan, R. C. (2009). Automated classification of visible and infrared spectra using cluster analysis. *Journal of Geophysical Research*, 114, E08001. <https://doi.org/10.1029/2008JE003250>

- McClintock, W. E., & Lankton, M. R. (2007). The Mercury atmospheric and surface composition spectrometer for the MESSENGER mission. *Space Science Reviews*, 131, 481–521. <https://doi.org/10.1007/s11214-007-9264-5>
- Murchie, S. L., Klima, R. L., Denevi, B. W., Ernst, C. M., Keller, M. R., Domingue, D. L., et al. (2015). Orbital multispectral mapping of Mercury with the MESSENGER Mercury Dual Imaging System: Evidence for the origins of plains units and low-reflectance material. *Icarus*, 254, 287–305. <https://doi.org/10.1016/j.icarus.2015.03.027>
- Namur, O., & Charlier, B. (2017). Silicate mineralogy at the surface of Mercury. *Nature Geoscience*, 10(1), 9–13. <https://doi.org/10.1038/ngeo2860>
- Nishizawa, T., Nakamura, H., Churikova, T., Gordeychik, B., Ishizuka, O., Haraguchi, S., et al. (2017). Genesis of ultra-high-Ni olivine in high-Mg andesite lava triggered by seamount subduction. *Scientific Reports*, 7(1), 11515. <https://doi.org/10.1038/s41598-017-10276-3>
- Nittler, L. R., Starr, R. D., Weider, S. Z., McCoy, T. J., Boynton, W. V., Ebel, D. S., et al. (2011). The major-element composition of Mercury's surface from MESSENGER X-ray spectrometry. *Science*, 333(6051), 1847–1850. <https://doi.org/10.1126/science.1211567>
- Pajola, M., Roush, T., Dalle Ore, C., Marzo, G. A., & Simioni, E. (2018). Phobos MRO/CRISM visible and near-infrared (0.5–2.5 μm) spectral modeling. *Planetary and Space Science*, 154, 63–71. <https://doi.org/10.1016/j.pss.2018.02.016>
- Peplowski, P. N., Evans, L. G., Hauck, S. A., McCoy, T. J., Boynton, W. V., Gillis-Davis, J. J., et al. (2011). Radioactive elements on Mercury's surface from MESSENGER: Implications for the planet's formation and evolution. *Science*, 333(6051), 1850–1852. <https://doi.org/10.1126/science.1211576>
- Peplowski, P. N., Lawrence, D. J., Feldman, W. C., Goldsten, J. O., Bazell, D., Evans, L. G., et al. (2015). Geochemical terranes of Mercury's northern hemisphere as revealed by MESSENGER neutron measurements. *Icarus*, 253, 346–363.
- Peplowski, P. N., Lawrence, D. J., Rhodes, E. A., Sprague, A. L., McCoy, T. J., Denevi, B. W., et al. (2012). Variations in the abundances of potassium and thorium on the surface of Mercury: Results from the MESSENGER gamma-ray spectrometer. *Journal of Geophysical Research*, 117, E00L04. <https://doi.org/10.1029/2012JE004141>
- Pinilla-Alonso, N., Roush, T. L., Marzo, G. A., Cruikshank, D. P., & Dalle Ore, C. M. (2011). Iapetus surface variability revealed from statistical clustering of a VIMS mosaic: The distribution of CO₂. *Icarus*, 215(1), 75–82. <https://doi.org/10.1016/j.icarus.2011.07.004>
- Prockter, L. M. (2016). The first global geologic map of Mercury, Lunar Planet. In Sci. Conf. 47, Abstract (Vol. 1245).
- Schlemm, C. E., Starr, R. D., Ho, G. C., Bechtold, K. E., Hamilton, S. A., Boldt, J. D., et al. (2007). The X-ray spectrometer on the MESSENGER spacecraft. In *The Messenger Mission to Mercury* (pp. 393–415). New York, NY: Springer. https://doi.org/10.1007/978-0-387-77214-1_11
- Solomon, S. C. (2011). A new look at the planet Mercury. *Physics Today*, Jan 2011, 64, 50–55.
- Solomon, S. C., McNutt, R. L., Gold, R. E., & Domingue, D. L. (2007). MESSENGER mission overview. *Space Science Reviews*, 131(1–4), 3–39. <https://doi.org/10.1007/s11214-007-9247-6>
- Spudis, P. D., & Guest, J. E. (1988). Stratigraphy and geologic history of Mercury. In *Mercury* (pp. 118–164).
- Thomas, R. J., Rothery, D. A., Conway, S. J., & Anand, M. (2014). Hollows on Mercury: Materials and mechanisms involved in their formation. *Icarus*, 229, 221–235. <https://doi.org/10.1016/j.icarus.2013.11.018>
- Vander Kaaden, K. E., & McCubbin, F. M. (2015). Exotic crust formation on Mercury: Consequences of a shallow, FeO-poor mantle. *Journal of Geophysical Research: Planets*, 120, 195–209. <https://doi.org/10.1002/2014JE004733>
- Vaughan, W. M., Helbert, J., Blewett, D. T., Head, J. W., Murchie, S. L., Gwinner, K. et al. (2012). Hollow-forming layers in impact craters on Mercury: Massive sulfide or chloride deposits formed by impact melt differentiation? In Lunar and Planetary Science Conference (Vol. 43).
- Vilas, F., Domingue, D. L., Helbert, J., D'Amore, M., Maturilli, A., Klima, R. L., et al. (2016). Mineralogical indicators of Mercury's hollows composition in MESSENGER color observations. *Geophysical Research Letters*, 43, 1450–1456. <https://doi.org/10.1002/2015GL067515>
- Weider, S. Z., Nittler, L. R., Starr, R. D., Crapster-Pregont, E. J., Peplowski, P. N., Denevi, B. W., et al. (2015). Evidence for geochemical terranes on Mercury: Global mapping of major elements with MESSENGER's X-ray spectrometer. *Earth and Planetary Science Letters*, 416, 109–120. <https://doi.org/10.1016/j.epsl.2015.01.023>
- Weider, S. Z., Nittler, L. R., Starr, R. D., McCoy, T. J., & Solomon, S. C. (2014). Variations in the abundance of iron on Mercury's surface from MESSENGER X-Ray Spectrometer observations. *Icarus*, 235, 170–186.
- Weider, S. Z., Nittler, L. R., Starr, R. D., McCoy, T. J., Stockstill-Cahill, K. R., Byrne, P. K., et al. (2012). Chemical heterogeneity on Mercury's surface revealed by the MESSENGER X-ray spectrometer. *Journal of Geophysical Research*, 117, E00L05. <https://doi.org/10.1029/2012JE004153>
- White, W. B., Mccarthy, G. J., & Scheetz, B. E. (1971). Optical spectra of chromium, nickel, and cobalt-containing pyroxenes. *American Mineralogist. Journal of Earth and Planetary Materials*, 56(1–2), 72–89.